J Nanostruct 10(1): 9-19, Winter 2020

RESEARCH PAPER

Pure and Gd^{3+}, Tb^{3+} and Ho^{3+}-Doped $As_2Ni_3O_8$: A New Visible Light Induced Photocatalyst for the Photodegradation of Malachite Green Water Pollutant

Alireza Hakimyfard [1], Nemat Tahmasebi [2], Mohammad Samimifar [2], Marzieh Naghizadeh [1]*

[1]*Department of Physics, Faculty of Science, Jundi-Shapur University of Technology, Dezful, Iran*

[2]*Department of Chemistry, Faculty of Science, Jundi-Shapur University of Technology, Dezful, Iran*

ARTICLE INFO

Article History:
Received 15 September 2019
Accepted : 24 October 201
Published : 01 January 2020

Keywords:
$As_2Ni_3O_8$
Malachite Green
Optical Property
Photocatalytic degradation

ABSTRACT

TNanostructured doped $As_2Ni_3O_8$ samples were synthesized via facile one step solid state reactions at 850 °C for 8 h using As_2O_3, $Ni(NO_3)_2.6H_2O$, Gd_2O_3, Tb_2O_3 and Ho_2O_3 raw materials. The synthesized nanomaterials were characterized by powder X-ray diffraction (PXRD) technique. The rietveld analyses showed that the obtained materials were crystallized well in monoclinic crystal structure with the space group $P12_1/c1$. The morphology of the synthesized materials was studied by field emission scanning electron microscope (FESEM). Photocatalytic performance of the as-synthesized sample was investigated for the degradation of pollutant Malachite Green (MG) in aqueous solution under direct visible light irradiation. The light source was a white color fluorescent lamp with the 40 W power and light intensity of 1.34 W/m^2 measured by a digital lux meter. The distance between the lamp and the surface of the solution was 50 cm. The degradation yield at the optimized condition (0.1 mL H_2O_2, 60 mg catalyst and 90 min) was 94 % for pure $Ni_3As_2O_8$.

How to cite this article
Hakimyfard AR, Tahmasebi N, Samimifar N, Naghizadeh M. Pure and Gd^{3+}, Tb^{3+} and Ho^{3+}-Doped $As_2Ni_3O_8$: A New Visible Light Induced Photocatalyst for the Photodegradation of Malachite Green Water Pollutant. J Nanostruct, 2020; 10(1): 9-19.
DOI: 10.22052/JNS.2020.01.002

INTRODUCTION

Nickel ortho-arsenate ($As_2Ni_3O_8$) is composed of two As^{5+} and Ni^{2+} cations. The compound has two crystal structures including orthorhombic and monoclinic structures. When the compound crystallizes in orthorhombic crystal system, the space group and lattice parameters are Cmca and a = 5.943, b = 11.263, and c = 8.164 Å, respectively. The space group and lattice parameters of the monoclinic crystal system are $P12_1/c1$ and a = 5.764, b = 9.559, and c = 10.194 Å, respectively. $As_2Ni_3O_8$ contains NiO and As_2O_5 in its crystal system. NiO is interested for its electrical, magnetic and catalytic properties. Nickel (II) oxide is used in several applications such as catalyst production, electrochromic films, fuel cell electrodes, gas sensors, and etc. [1-5]. As_2O_3 is used in some fields including wood reservoir, and production of arsenic organic materials for various applications [6-7]. Hydrothermal [8] and solid state [9] methods have been reported for the synthesis of $As_2Ni_3O_8$ material.

A photocatalytic application for removing MG from aqueous waste is reported in the present work. MG is classified in the dyestuff industry as a triarylamine dye and used in pigment industry. MG is used as an antifungal and anti-protozoan agent in fisheries and aquaculture industry [10]. However, MG causes mutagenic, carcinogenic, and teratogenic effects to living organisms [11]. MG causes skin irritation, blurred vision or cause interference. MG inhalation may cause irritation to the respiratory tract, and in large quantities can cause tissue damage and inflammation of kidney

* *Corresponding Author Email: ahakimyfard@jsu.ac.ir*
ahakimyfard@yahoo.com

[12,13]. So, we decided to study the performance of the semiconductor nanomaterial for the degradation of MG. Several metal oxides and sulfides have been used for the degradation of MG under different conditions summarized in ref [14].

In the present study, a facile solid state rout is applied for the first time to synthesize Gd^{3+}, Tb^{3+} and Ho^{3+}-doped $As_2Ni_3O_8$ powders using As_2O_3, $Ni(NO_3)_2.6H_2O$, Gd_2O_3, Tb_2O_3 and Ho_2O_3 at 850 °C for 8 h. To the best of our knowledge, there is no report on the synthesis of $As_2Ni_3O_8$ doped nanomaterials in the literature. Rietveld analysis was used to find the experimental crystallographic data of the as-prepared targets. The morphology of the obtained targets was studied by FESEM. The photocatalytic application of the synthesized doped $As_2Ni_3O_8$ nanomaterials was investigated for the first time for the degradation of MG under direct visible light irradiation. Experimental design method was used to optimize the factors affecting the degradation process.

MATERIALS AND METHODS

General remarks

All chemicals were of analytical grade, obtained from commercial sources, and used without further purification. Phase identifications were performed on a powder X-ray diffractometer D5000 (Siemens AG, Munich, Germany) using CuKα radiation. The morphology of the obtained materials was examined by a field emission scanning electron microscope (Hitachi FE-SEM model S-4160). The elemental analyses of the obtained materials were examined with a Philips XL30 scanning electron microscope (Philips, Amsterdam, Netherlands). The concentration of MG was determined at 612 nm using a Shimadzu UV-visible1650 PC spectrophotometer. A BEL PHS-3BW pH-meter with a combined glass-Ag/AgCl electrode was used to adjust the solution pH value. A digital Lux meter model GM 1010 was used to measure the light intensity used in the photocatalytic process.

To prepare 70 ppm of MG solution, 70 mg of MG powder was dissolved in 1000 mL of distilled water. The pH value of the obtained solution was 4. To increase and decrease the pH value, 0.01 M solutions of NaOH and HCl, respectively, were used. In a typical experiment, certain amount (g) of the as-synthesized pure $As_2Ni_3O_8$ photocatalyst was added into 100 mL of MG solution and sonicated for 10 min in a dark room to establish an adsorption/desorption equilibrium between MG molecules and the surface of the photocatalyst. Afterwards, certain volume (mL) of H_2O_2 was added into the mixture solution followed by further magnetic stirring under visible light irradiation. When the designed time (min) was elapsed, the solution was drawn out and the photocatalyst was separated by centrifugation in order to measure the absorption spectrum of MG and calculate the MG concentration by UV-Vis spectroscopy. The photodegradation percentage of MG was calculated by the following formula:

$$\left(\frac{\mathbf{A}_0 - \mathbf{A}_t}{\mathbf{A}_0}\right)\times 100 \quad (1)$$

where, A_0 and A_t represent the initial absorbance of MG at 616 nm and the absorbance at time t, respectively.

Synthesis of Gd^{3+}, Tb^{3+} and Ho^{3+} $As_2Ni_3O_8$ nanomaterials

The synthesis rout is according to our previously reported work [9]. In a typical synthetic solid state experiment, 0.198 g (1 mmol) of As_2O_3 (MW = 197.8 $gmol^{-1}$) and 0.297 g (1 mmol) of $Ni(NO_3)_2.6H_2O$ (MW = 290.7 $gmol^{-1}$) 0.05 mmol of Gd_2O_3 (S_1) or Tb_2O_3 (S_2) or Ho_2O_3 (S_3) were mixed in a mortar and ground until a nearly homogeneous powder was obtained. The obtained powder was added into a 25 mL crucible and treated thermally in one step at 850 °C for 8 h. When the reaction was completed, the crucible was cooled normally in the furnace to the room temperature.

RESULTS AND DISCUSSIONS

Characterization

The phase composition of S_1, S_2 and S_3 were examined by powder X-ray diffraction technique. Fig. 1(a-d) shows the PXRD patterns of the obtained materials in the 2θ range 10-90° as well as the structural analyses performed by the *FullProf* program. The structural analyses were performed employing profile matching with constant scale factors. Red lines are the observed intensities; the black ones are the calculated data; the blue ones are the difference: Y_{obs}-Y_{calc}; and the Bragg reflections positions are indicated by blue bars for monoclinic phase of $As_2Ni_3O_8$ [9]. The results showed that the patterns had a main $As_2Ni_3O_8$ crystal structure with the space group $P12_1/c1$ [8,9]. The ionic radii of the component ions are

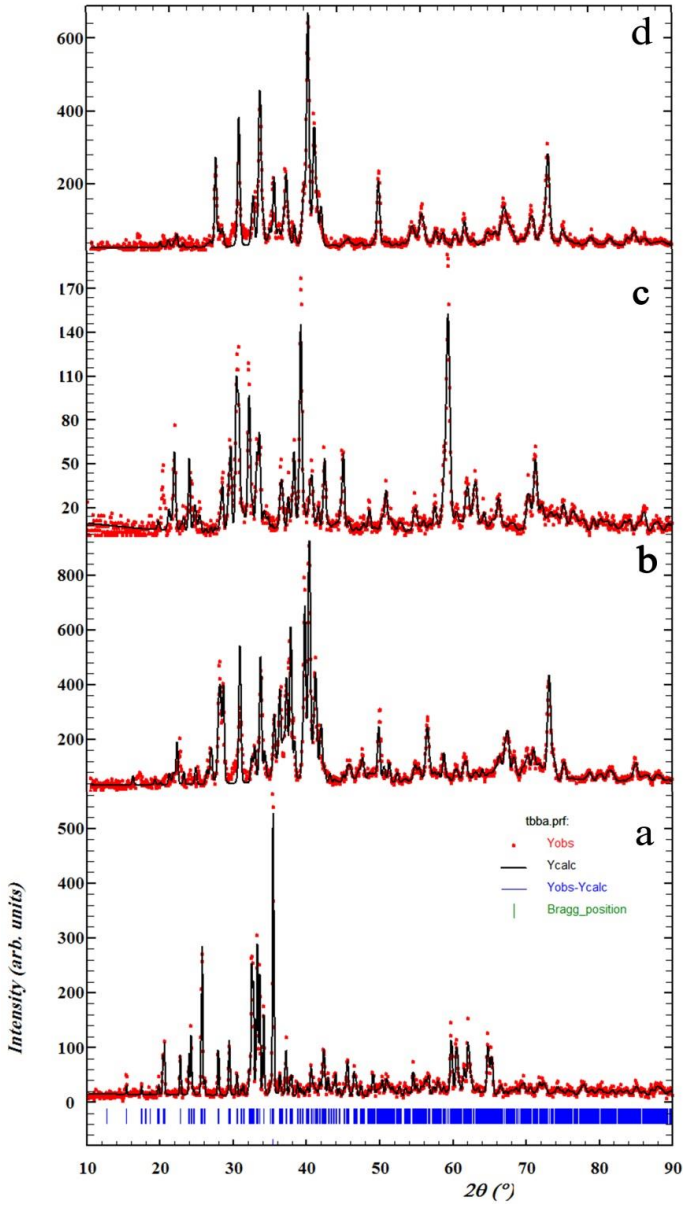

Fig. 1. PXRD patterns of a) pure $Ni_3As_2O_8$, b) S_1, c) S_2 and d) S_3.

as follow: Ni^{2+} (CN=6): 0.69 Å, As^{5+} (CN=4): 0.34 Å, As^{5+} (CN=6): 0.46 Å, Gd^{3+} (CN=6): 0.94, Tb^{3+} (CN=6): 0.92, Ho^{3+} (CN=6): 0.91 Å [15].

Quantitative phase analysis was investigated with direct comparison method [16]. In this method, we compared the experimental line intensity of the impurity phases $SrCO_3$ for S_1 and S_3, and $SrCO_3$ and As_2O_3 for S_2 from the mixture to a line from the main phase ($As_2Ni_3O_8$) in the mixture. For this purpose, we chose the peaks with highest intensity for each phase at about 26.8˚, 29.8 and 37.6˚ for As_2O_3, $SrCO_3$ and $As_2Ni_3O_8$, respectively. The phase comparison values are summarized in Table 1. Table 1 shows that the purity and crystal phase growth of the samples are decreased more when Tb^{3+} is doped into the crystal system. As will be mentioned in Table 2, the dislocation density and strain values are increased by decreasing the crystallite size value.

The cell parameters values were calculated and refined by the rietveld analysis. According to the lattice volume data, it is clear that introducing the lanthanide ions into the crystal system has decreased the lattice size. However, the decreasing

Table 1. Crystallographic data of the obtained materials.

Sample	A	b	c	V	β	Purity	Counts
Pure	5.76449	9.54642	10.18623	559.822	92.94801	100	568
S_1	5.73286	9.47594	10.05626	545.5885	92.89967	78	997
S_2	5.72701	9.57578	10.11208	553.8315	92.90769	67	194
S_3	5.75738	9.44057	10.08413	547.3897	92.91501	84	687

Table 2. Crystallite size, dislocation density, strain, and interplanar spacing data of the as-synthesized nanomaterials.

	2θ	θ	B (º)	B(rad)	cosθ	sinθ	D	δ	ε	d_{Bragg}	d_{hkl}
Pure	35.26	17.63	0.19067	0.003326	0.953	0.303	44	5.23	0.79242	2.54	2.55
S_1	35.76	17.88	0.31619	0.005516	0.952	0.307	26	14.35	1.312808	2.51	2.51
S_2	35.53	17.76	0.39571	0.006903	0.952	0.305	21	22.48	1.642914	2.52	2.53
S_3	35.63	17.81	0.34989	0.006104	0.952	0.306	24	17.58	1.452752	2.52	2.52

for Tb^{3+} doped material is lower than the other samples.

Table 2 shows the crystallite size data, dislocation density, strain and interplanar spacing (d) data for S_1 to S_3. The crystallite size data of the obtained nanomaterials is calculated by Scherrer equation (1):

$$D = \frac{K\lambda}{B_{\frac{1}{2}} cos\theta} \quad (1)$$

In this equation, D is the entire thickness of the crystalline sample, λ is the X-ray diffraction wavelength (0.154 nm), K is the Scherrer constant (0.9), $B_{1/2}$ of FWHM is the full width at half of its maximum intensity and θ is the half diffraction angle at which the peak is located. The crystallite size data show that the dopant type plays an important role to produce particles in nanometer size scale. The data included in Table 2 show that the crystallite sizes are decreased more when Tb_2O_3 is used as the dopant source.

The value of the dislocation density δ [(lines/m^2)10^{14}], which is related to the number of defects in the crystal was calculated from the average values of the crystallite size (D) by the relationship given below [17]:

$$\delta = \frac{1}{D^2}$$

It was found that the dislocation density was increased when the dopant ions were introduced into the crystal system. However, the data show that doping Tb^{3+} ion into the crystal cavity increases more the dislocation density due to the decreasing the crystallite sizes of the materials. The strain ε (10^{-3}) values were determined with by the following formula:

$$\varepsilon = \frac{\beta_{hkl} cos\theta}{4}$$

The variation in the strain as a function of the dopant ion type is included in Table 2. Increase in the strain value with changing the dopant ion is probably due to the retrograde in the degree of the crystallite of the obtained target. However, when Tb^{3+} is doped into the crystal system, the strain value is increased more.

The interplanar spacing data of the obtained monoclinic samples were also calculated and compared to the observed data.

$$\frac{1}{d^2} = \frac{1}{sin^2\beta}\left(\frac{h^2}{a^2} + \frac{k^2 sin^2\beta}{b^2} + \frac{l^2}{c^2} - \frac{2hl\cos\beta}{ac}\right)$$

The highest intensity peak with the (h k l) value of (004) at 2θ=35.26 was used in the above equation.

As we know, *sin* (92.9) is about 0.999. So,

$$\frac{1}{d^2} = \left(\frac{16}{c^2}\right)$$

Besides, the unit cell volume can be obtained from the below formula:

$$V = a.b.c.sin(\beta)$$

Where a, b and c are the lattice parameters and *V* is the cell volume.

Morphology analysis

Fig. 2 shows the FESEM images of the obtained nanomaterials. The images show that the

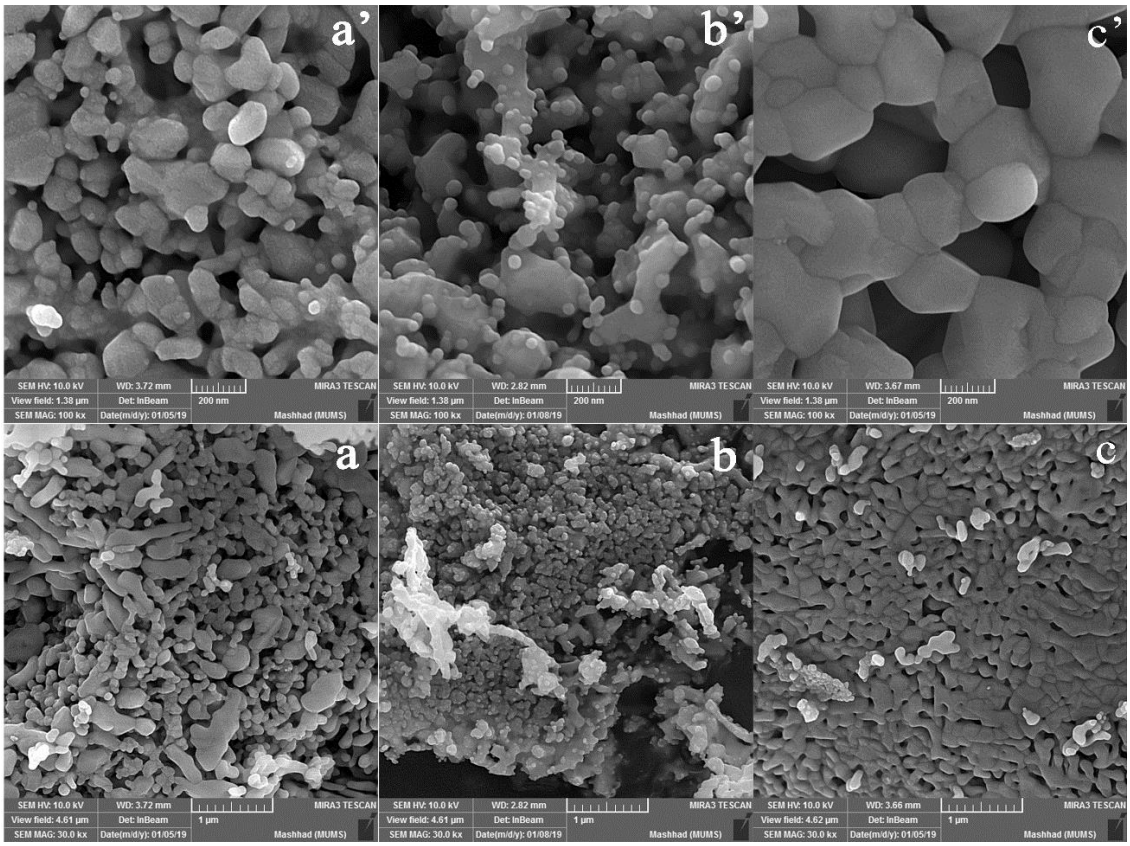

Fig. 2. FESEM images of a,a') S_1, b,b') S_2 and c,c') S_3.

morphology of the targets is sponge. However, the data indicate that the sponge structure of the obtained doped nanomaterials is different from the pure $Ni_3As_2O_8$ [9]. This difference is due to doping the lanthanide ions into the crystal system. It is obvious from the images that when Gd^{3+} and Tb^{3+} are doped into the crystal system, some particles are observed on the surface of the sponge. But this observation is not seen for Ho^{3+} doped material. The particle size on the surface of the sponge is about 40 nm.

Fig. 3a - c illustrates the EDX analyses for the samples doped theoretically with 0.05 mmol of the lanthanide dopants ions into the crystal system which verify the doping and the compositional analysis of Gd^{3+} or Tb^{3+} and/or Ho^{3+} in $Ni_3As_2O_8$. The peaks corresponded to Gd or Tb or Ho and (Ni, As and O) atoms present in the samples are labeled. The respective energy positions and the specific X-ray lines from various elements are also indicated. The A% values of the dopants in the obtained samples and investigating the capacity of the sample to accept the ions in the crystal systems is reported. The A% values are 0.82, 0.79 and 0.78 for Gd^{3+}, Tb^{3+} and Ho^{3+} doped nanomaterials. The data reveal that when a heavier lanthanide ion is included in the crystal system, the capacity of the crystal system to accept the ions is decreased.

Photocatalytic activity

Experimental design for achieving optimal conditions in MG degradation process

Experimental design approach is attracting attention in the literature for exploring the optimal level of factors affecting chemical reactions. One of the most common designs is full factorial design. Response surface methodology (RSM) is a mathematical and statistical method, which analyzes experimental design by applying an empirical model. The adequacy of the applied model is checked using analysis of variance (ANOVA) which needs some replicate experiments. The response is the measured degradation yield (Y%). Different possible combinations of these factors are designed which are collected in table 3. The observed data of the factorial design was

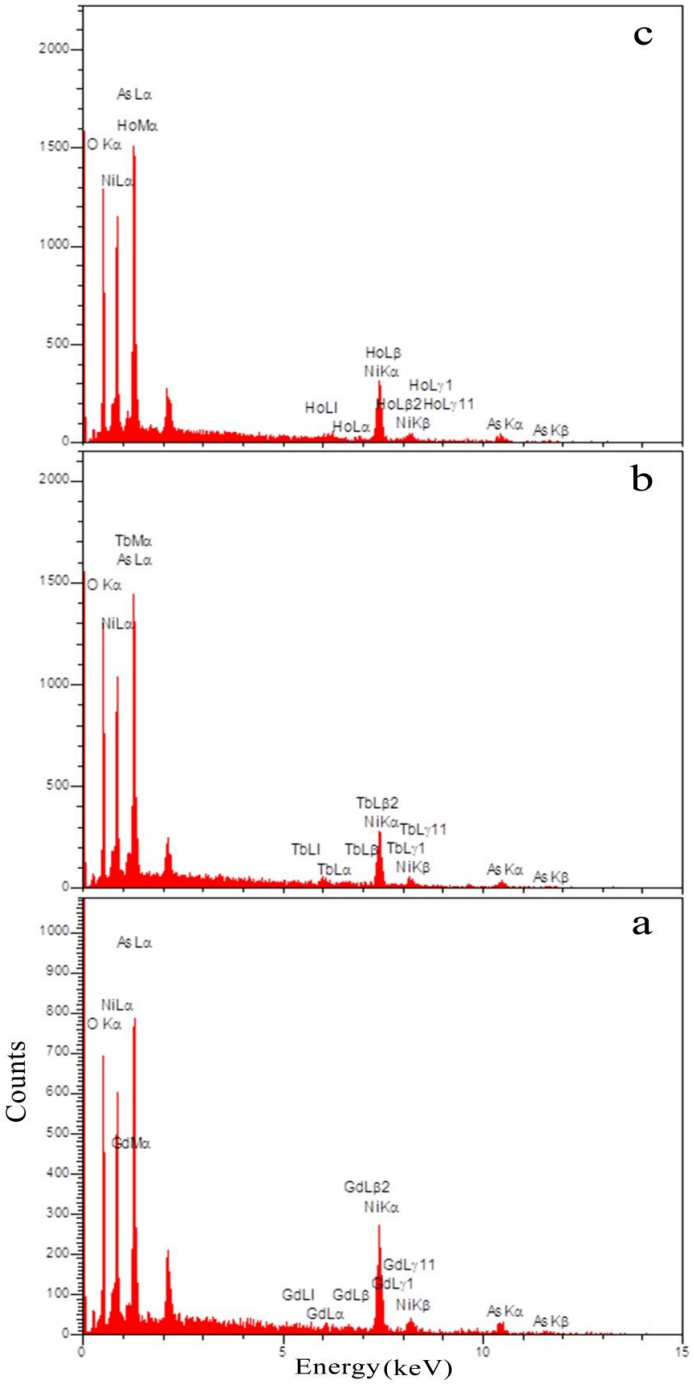

Fig. 3. EDX graphs of a) S_1, b) S_2 and c) S_3.

Table 3. Three-level full factorial design in photodegradation process.

Sample	A	b	c	V	β	Purity	Counts
Pure	5.76449	9.54642	10.18623	559.822	92.94801	100	568
S_1	5.73286	9.47594	10.05626	545.5885	92.89967	78	997
S_2	5.72701	9.57578	10.11208	553.8315	92.90769	67	194
S_3	5.75738	9.44057	10.08413	547.3897	92.91501	84	687

Table 4. The experimental range and levels of independent variables in CCD.

	Factor	Low	High	Low coded	High coded
A	catalyst	30	60	-1	1
B	H_2O_2	0.05	0.1	-1	1
C	Time	60	90	-1	1

Table 5. Analysis of variance for suggested model.

Source	Sum of Squares	df	Mean Square	F Value	p-Value Prob > F	
Model	8320.67	3	2773.56	196.46	< 0.0001	significant
A-catalyst	5271.62	1	5271.62	373.41	< 0.0001	
B-H_2O_2	2673.77	1	2673.77	189.4	< 0.0001	
C-Time	375.28	1	375.28	26.58	< 0.0001	
Residual	225.88	16	14.12			
Lack of Fit	204.54	11	18.59	4.36	0.0582	not significant
Pure Error	21.33	5	4.27			
Cor Total	8546.55	19				

fitted to a linear response model. The below equation shows the relation between the factors and the yield, Y%, based on the first order model:

$$Y\ (\%) = 55.35 + 19.65 \times \text{Catalyst} + 13.99 \times H_2O_2 + 5.24 \times \text{Time}$$

Prior to the ANOVA analysis, low and high factor levels were coded to -1 and +1, respectively (Table 4). As could be seen from the ANOVA results listed in table 5, the p-value of the regression is smaller than 0.05. This indicates that the model is significant at a high level of confidence (95%). The p-value probability of lack of fit is also greater than 0.05, which confirms the significance of the model. Also the coefficient of determination (the R-square, adjusted–R-square) was used to express the quality of fit of polynomial model equation. In this case, R^2 value of variation fitting for Y% = 94 indicated a high degree of correlation between the response and the independent factors (R^2 = 0.97). The high value of adjusted regression coefficient (R^2-adj = 0.90) was also another index for the high significance of the proposed model. This means that the difference between the experimental and predicted responses is negligible. The dispersal of residuals is also shown in Fig. 4. As it is evident in this figure, the data points obtained consistently appear on a straight trend line, demonstrating that there is no obvious dispersal. It is clear that the residuals are in the range of -3 to +3 confirming more the reliability of the model.

To illustrate the effects of the factors in the above models, the two and three–dimensional (3D) response surface plot of the response (when the time was fixed at optimal level and the other two were allowed to vary) is shown in Fig. 5. The figure represents the 3D and counter plots related to the interaction of AB.

Fig. 6 shows the optimum values of the parameters involving in the MG degradation process obtained by the mentioned model. The data show that the optimum values for catalyst, H_2O_2 and time are 60 mg, 0.10 mL and 90 min, respectively.

A three-level CCD (Central Composite Design) with three factors (catalyst (A), H_2O_2 (B) and time (C)) was used to investigate the effects of the factors. The condition of 20 experiments designed by CCD accompanied to dye degradation percentage (response (R%)) are also given in Table 3. As shown in table 4, the independent variables (H_2O_2 volume (A), catalyst amount (B) and stirring time (C)) are given the coded form (-α, -1, 0, +1, +α).

Fig. 7 shows the dye degradation graphs for the obtained materials at the optimum conditions. Fig. 7 a shows the effect of solution pH on the degradation yield. It is clear that by increasing the pH value, the degradation of dye is increased. The data reveal data the existance of H^+ ion decreases the degradation yield. But, when the concentration of H^+ is decreased or the concentration of OH^- is increased, the degradation yield is increased considerably. Fig. 7b shows the reusability test for the as-prepared catalyst in the photodegradation process. It indicates that the degradation is high until run 4. Fig. 7c presents the dye solution volume influence on the photodegradation yield. The data indicate that when the dye volume is increased more up to 140 mL, the yield is still

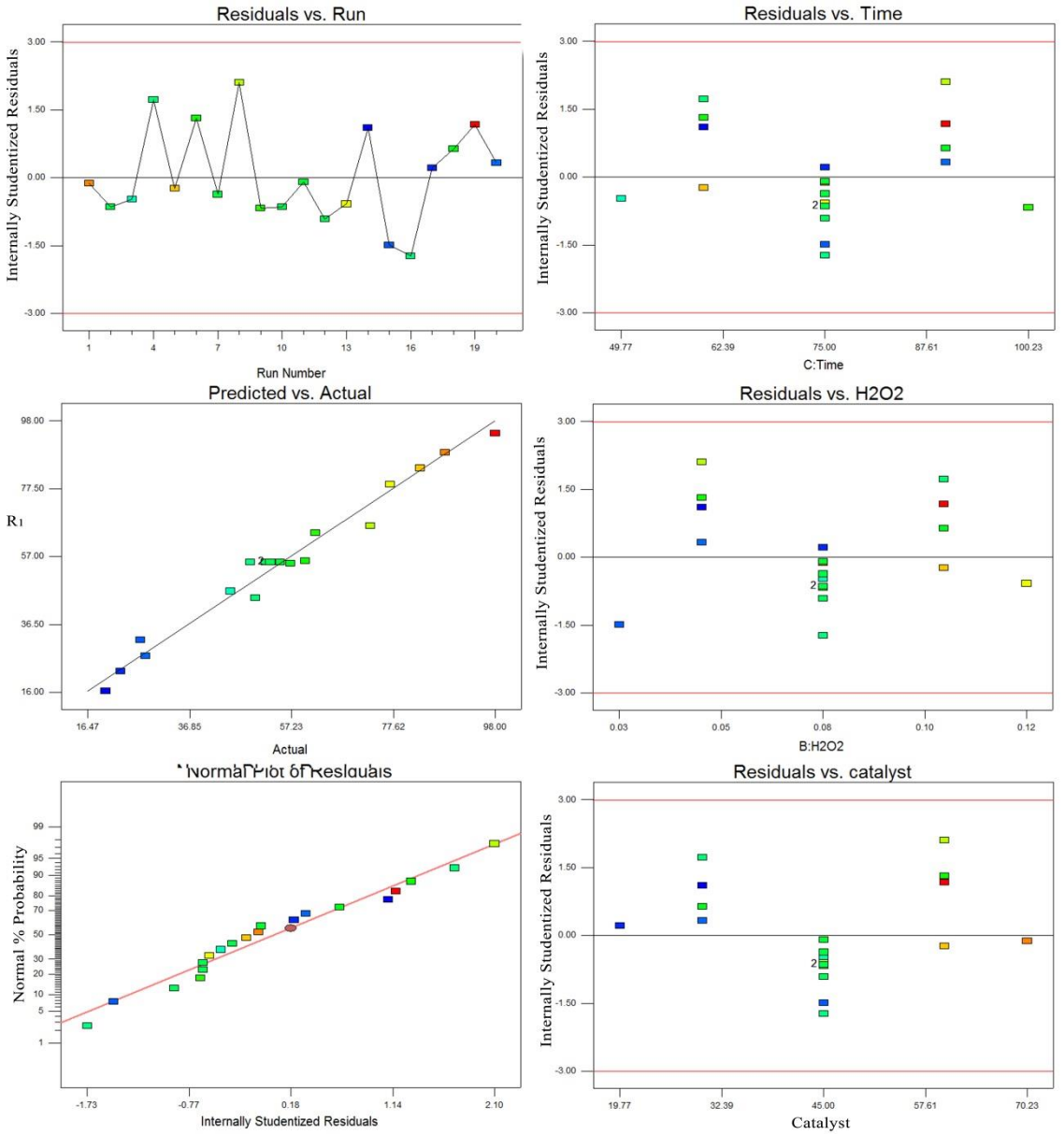

Fig. 4. Normalized plot of residual, experimental data versus the predicted data of normalized removal of dye and dispersal residuals plots.

desirable. However, when the solution volume is increased more, the degrataion yield is decreased considerably. It is due to the decreasing the adsorption of dye on the catalyst; so the process is continued slowly at the desired time. Fig. 7d shows the effect of the dye concentration influence on the degradation yield. According to the data, it is clear that with increasing the dye concentration to 80 ppm, the degradation yield is decreased by about 20 %. The observation indicates that increasing the dye concentration has a main effect on the retrograding the degradation yield and the process is related to the concentration of the dye, considerably.

We present a copmarison study to show the merit of the present work with the other reported photocatalytic degradation researches (table 6).

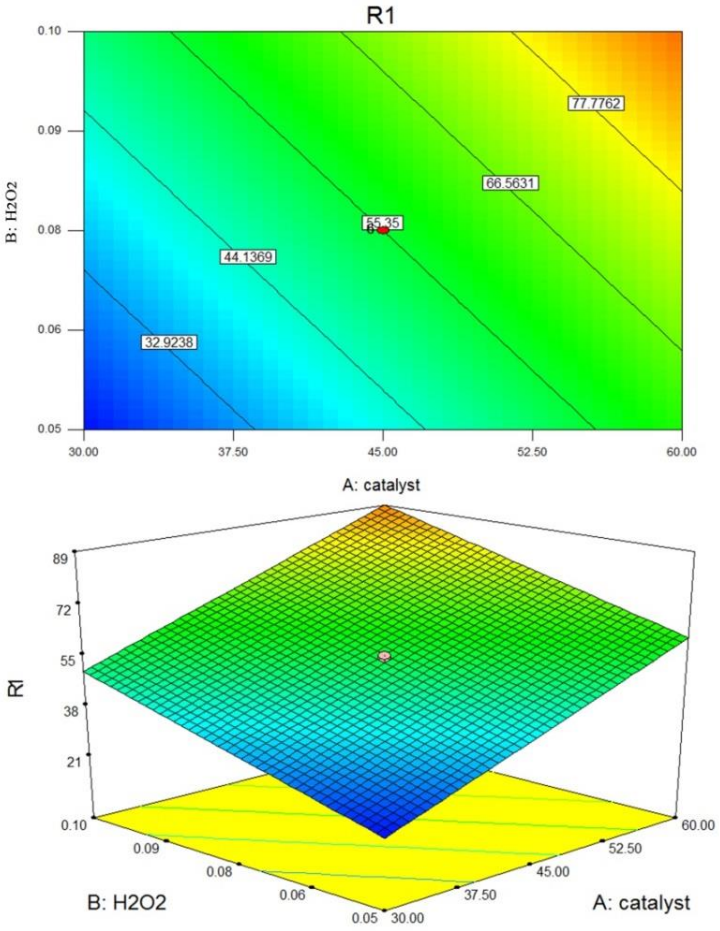

Fig. 5. 2 D and 3D plots of MG dye removal.

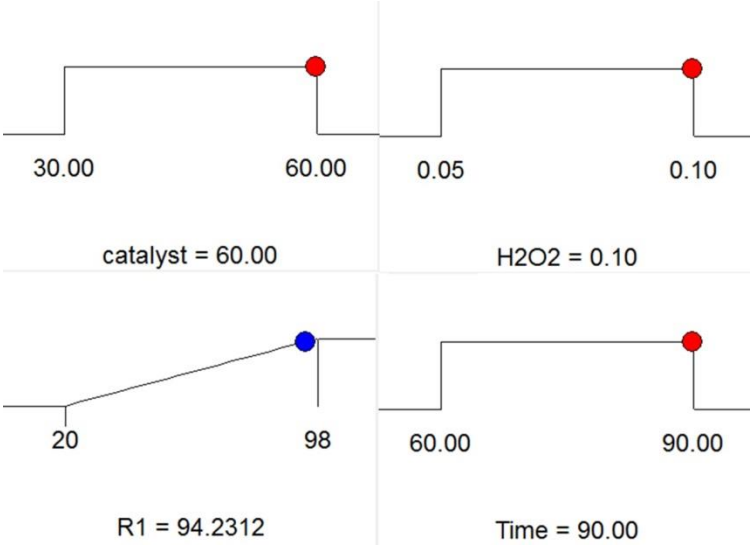

Fig. 6. The optimized values of the photocatalytic degradation.

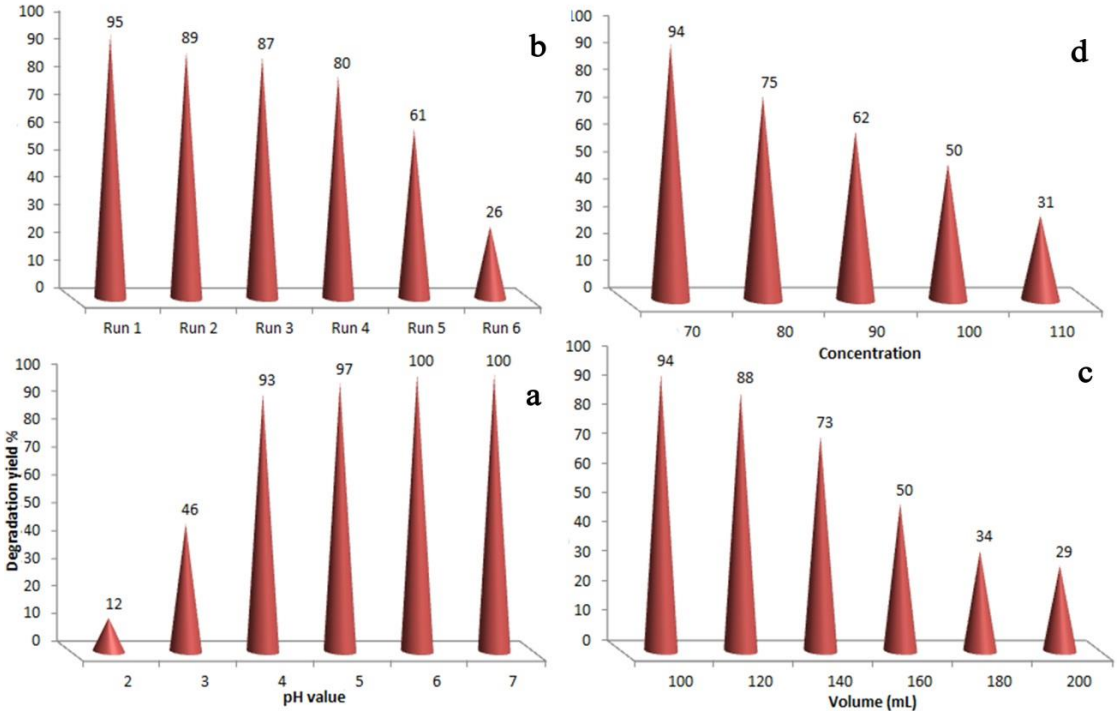

Fig. 7. MG degradation (%) at different (a) dye pH values, (b) reusability for S_1, (c) dye concentrations, (d) dye volumes.

Table 6. Comparison study for the degradation efficiency [14].

Catalyst	Condition	Yield (%)
Carbon/TiO_2	25 ppm MG, 30 min, pH=8	82-100
MoS_2/TiO_2	40 min, sunlight irradiation, 0.1 g catalyst, 10 ppm MG	97
$PbCrO_4$	365 ppm MG, 0.1 g catalyst, 4 h, pH=7.5, visible light, 60 min	90
V doped-ZnO	UV and visible lights, 500 ppm MG, 500 ppm catalyst, 200 min	90
$Ni_{1-x}Co_xFe_2O_4$	Sunlight, 50 mL solution, 25 ppm catalyst, 1 µM MG, H_2O_2, 15 h	100
Mg-doped TiO_2	Visible light, pH=9, 100 ppm MG	89
ZnO	4h time, 60 ppm MG, pH=7.5, solar radiation	98
$FeSO_4$ -$7H_2O$	10 mM Fe^{2+}, 40 °C, 25.5mM H_2O_2, 10 ppm MG	94
$Sr_2As_2O_7$	H_2O_2, 20 mg catalyst, 33 min, 70 mL of 100 ppm MG, solar light	97
$MgFe_2O_4$	H_2O_2 , 25 mg catalyst, 40 min, 80 mL of 100 ppm MG, visible light	100
$Ni_3As_2O_8$	H_2O_2, 60 mg catalyst, 90 min, 100 mL of 70 ppm MG, visible light (Present Work)	94

CONCLUSION

In this work, Gd^{3+}, Tb^{3+} and Ho^{3+}-doped $Ni_3As_2O_8$ nanomaterial was synthesized via a facile solid state method. PXRD patterns and structural analyses done by the *FullProf* program employing profile matching. The rietveld analyses showed that the obtained materials were crystallized well in monoclinic crystal structure with the space group $P12_1/c1$. FESEM images showed the obtained materials had sponge morphology. The data showed that doping the lanthanid ions into the crystal system affect on the morphology of the obtained nanomaterials. The photocatalytic degradation data showed that $Ni_3As_2O_8$ had excellent efficiency for the removal of MG from aqueous solution. It was found that the optimum condition was 0.1 mL H_2O_2, 60 mg catalyst and 90 min for the removal of 100 mL of 70 ppm MG solution. The degradation yield in these conditions was 94 % for pure $Ni_3As_2O_8$.

CONFLICT OF INTEREST

The authors declare that there is no conflict of interests regarding the publication of this manuscript.

REFERENCES

1. El-Kemary M, Nagy N, El-Mehasseb I. Nickel oxide nanoparticles: Synthesis and spectral studies of interactions with glucose. Materials Science in Semiconductor Processing. 2013;16(6):1747-52.
2. Rahdar A, Aliahmad M, Azizi Y. NiO Nanoparticles: Synthesis and Characterization. Journal of Nanostructures. 2015; 5: 145-151.
3. Riazian M. Internation. **Synthesis and nano structural study on TiO_2-NiO-SiO_2 composite**.

Int J Nano Dimens. 2014; 5: 123-131.

4. Zahraei F, Rahimi K, Yazdani A. **Preparation and characterization of Graphene/Nickel Oxide nanorods composite**. Int J Nano Dimens. 2015; 6: 371-376.
5. Khanahmadzadeh S, Barikan F. **Fabrication and magnetic properties of Polyimide/Nickel Oxide nanocomposite**. Int J Nano Dimens. 2014; 5: 365-370.
6. Grund SC, Hanusch K, Wolf HU. Arsenic and Arsenic Compounds. Ullmann's Encyclopedia of Industrial Chemistry: Wiley-VCH Verlag GmbH & Co. KGaA; 2000.
7. Gibaud S, Jaouen G. Arsenic-Based Drugs: From Fowler's Solution to Modern Anticancer Chemotherapy. Topics in Organometallic Chemistry: Springer Berlin Heidelberg; 2010. p. 1-20.
8. J. Barbier, C. Frampton, Acta Crystallographica, Section B., 47, 457 (1991).
9. Hakimyfard A, Khademinia S, Rahimkhani M, Solid state synthesis, crystal structure, evaluation of direct and indirect band gap energies and optimization of reaction parameters for $As_2Ni_3O_8$ nanomaterials. J Nanoanalysis. DOI: 10.22034/JNA.2018.561205.1073.
10. Tolia J, Chakraborty M, Murthy Z. Photocatalytic degradation of malachite green dye using doped and undoped ZnS nanoparticles. Polish Journal of Chemical Technology. 2012;14(2).
11. Kusuma H.S, Sholihuddin R.I, Harsini M, Darmokoesoemo H. Electrochemical Degradation of Malachite Green Dye using Carbon/TiO_2 Electrodes. Pol. J. Chem. Technol. 2016; 7: 1454-1460.
12. Hu K-H, Meng M. Degradation of Malachite Green on MoS2/TiO2 Nanocomposite. Asian Journal of Chemistry. 2013;25(10):5827-9.
13. Khademinia S, Behzad M, Kafi-Ahmadi L, Hadilou S. Hydrothermally Synthesized Strontium Arsenate Nanomaterial through Response Surface Methodology. Zeitschrift für anorganische und allgemeine Chemie. 2018; 644: 221-227.
14. Parvarinezhad S, Salehi M, Kademinia S. Solid state synthesis of $MgAl_2O_4$ nanomaterials and solar light-induced photocatalytic removal of Malachite green. Int J Nano Dimens. 2019; 10: 89-104.
15. Lide D R (2006) CRC Handbook of Chemistry and Physics, Internet Version, pages 1803-1804.
16. Kauffer E, Masson A, Moulut J C, Lecaque T, Protois J C (2005) Ann Occup Hyg 49: 661–671.
17. Mohammed RY, Abduol S, Mousa AM. Structural and Optical Properties of Chemically Deposited CdS Thin Films. International Letters of Chemistry, Physics and Astronomy. 2014;29:91-104.